Elasto-viscoplastic self consistent modeling of the ambient temperature plastic behavior of periclase deformed up to 5.4 GPa

F. Lin, N. Hilairet, P. Raterron, A. Addad, J. Immoor, H. Marquardt, C. N. Tomé, L. Miyagi, and S. Merkel

Citation: Journal of Applied Physics **122**, 205902 (2017);
View online: https://doi.org/10.1063/1.4999951
View Table of Contents: http://aip.scitation.org/toc/jap/122/20
Published by the American Institute of Physics

Elasto-viscoplastic self consistent modeling of the ambient temperature plastic behavior of periclase deformed up to 5.4 GPa

F. Lin,[1] N. Hilairet,[2] P. Raterron,[2] A. Addad,[2] J. Immoor,[3] H. Marquardt,[3] C. N. Tomé,[4] L. Miyagi,[1] and S. Merkel[2]
[1]*Department of Geology and Geophysics, University of Utah, Salt Lake City, Utah 84112, USA*
[2]*Univ. Lille, CNRS, INRA, ENSCL, UMR 8207, UMET—Unité Matériaux et Transformations, F-59000 Lille, France*
[3]*Bavarian Research Institute of Experimental Geochemistry and Geophysics, University Bayreuth, 95440 Bayreuth, Germany*
[4]*Materials Science and Technology Division, Los Alamos National Laboratory, Los Alamos, New Mexico 87545, USA*

(Received 11 August 2017; accepted 6 November 2017; published online 30 November 2017)

Anisotropy has a crucial effect on the mechanical response of polycrystalline materials. Polycrystal anisotropy is a consequence of single crystal anisotropy and texture (crystallographic preferred orientation) development, which can result from plastic deformation by dislocation glide. The plastic behavior of polycrystals is different under varying hydrostatic pressure conditions, and understanding the effect of hydrostatic pressure on plasticity is of general interest. Moreover, in the case of geological materials, it is useful for understanding material behavior in the deep earth and for the interpretation of seismic data. Periclase is a good material to test because of its simple and stable crystal structure (B1), and it is of interest to geosciences, as (Mg,Fe)O is the second most abundant phase in Earth's lower mantle. In this study, a polycrystalline sintered sample of periclase is deformed at ~5.4 GPa and ambient temperature, to a total strain of 37% at average strain rates of 2.26×10^{-5}/s and 4.30×10^{-5}/s. Lattice strains and textures in the polycrystalline sample are recorded using *in-situ* synchrotron x-ray diffraction and are modeled with Elasto-Viscoplastic Self Consistent (EVPSC) methods. Parameters such as critical resolved shear stress (CRSS) for the various slip systems, strain hardening, initial grain shape, and the strength of the grain–neighborhood interaction are tested in order to optimize the simulation. At the beginning of deformation, a transient maximum occurs in lattice strains, then lattice strains relax to a "steady-state" value, which, we believe, corresponds to the true flow strength of periclase. The "steady state" CRSS of the $\{110\}\langle 1\bar{1}0\rangle$ slip system is 1.2 GPa, while modeling the transient maximum requires a CRSS of 2.2 GPa. Interpretation of the overall experimental data via modeling indicates dominant $\{110\}\langle 1\bar{1}0\rangle$ slip with initial strain softening, followed by strain hardening. This approach illustrates the utility of combining EVPSC and experimental data to understand deformation of materials at high pressures. *Published by AIP Publishing*. https://doi.org/10.1063/1.4999951

I. INTRODUCTION

Considerable work has been performed to understand deformation mechanisms of materials under extreme conditions, especially high pressure. This topic is relevant for constraining material behavior inside the Earth and planets. It is also of general importance to understand the effect of hydrostatic pressure on the fundamentals of plasticity. Periclase has emerged as a model material for extreme conditions plasticity experiments (e.g., Merkel *et al.*, 2002 and Girard *et al.*, 2012) due to its simple rocksalt crystal structure (B1) that is stable to pressures in excess of 400 GPa (Coppari *et al.*, 2013). In the geosciences, deformation behavior of periclase is of importance because it is the magnesium end-member of (Mg,Fe)O ferropericlase, the second most abundant mineral in the Earth's lower mantle (Ringwood, 1991). For a simple oxide, periclase may exhibit complex deformation behavior under pressure. Theoretical calculations (Amodeo *et al.*, 2012) and single crystal deformation experiments (Girard *et al.*, 2012) suggest a pressure-induced inversion in slip system strength. Under high pressures, minerals deform plastically by dislocation glide over a wide range of conditions. Dislocation glide leads to texture (crystallographic preferred orientation) development, which results in anisotropic physical properties in polycrystalline materials. Much research in Earth science has focused on deformation and texture development in lithosphere and upper mantle materials, such as quartz (Wenk *et al.*, 2006), calcite (Barber *et al.*, 2007), and olivine (Zhang *et al.*, 2000). In contrast, considerably less is known about the deformation mechanisms of the materials in the deep mantle. Due to its stability at ambient conditions, deformation of ferropericlase (and periclase) has been studied in greater detail than other lower mantle phases (e.g., Stretton *et al.*, 2001; Heidelbach *et al.*, 2003; Uchida *et al.*, 1996; Uchida *et al.*, 2004; Yamazaki and Karato, 2002; Long *et al.*, 2006; Merkel *et al.*, 2002; and Marquardt and Miyagi, 2015). From these studies, it has been inferred that $\{110\}\langle 1\bar{1}0\rangle$ and $\{100\}\langle 011\rangle$ slip systems dominate in

periclase and ferropericlase. Many studies, including both experiments (Appel and Wielke, 1985; Sato and Sumino, 1980; Sinha *et al.*, 1973; and Hulse and Pask, 1960) and theoretical calculations (Amodeo *et al.*, 2011 and Cordier *et al.*, 2012), have investigated the yield strength of MgO single crystals under varying temperature and pressure conditions. In particular, numerical models of dislocation cores predict a transition from $\{110\}\langle 1\bar{1}0\rangle$ to $\{100\}\langle 011\rangle$ at pressures of approximately 50 GPa. Experiments on single crystals up to 8 GPa showed a different effect of pressure on the strength of the two slip systems, indicating that $\{100\}\langle 011\rangle$ slip may become easier than $\{110\}\langle 1\bar{1}0\rangle$ slip at a pressure of ~23 GPa (Girard *et al.*, 2012). The effect of this transition in polycrystalline periclase remains under investigation (e.g., Amodeo *et al.*, 2016). In general, deformation experiments on periclase polycrystals (Kinsland and Bassett, 1977; Duffy *et al.*, 1995; Paterson and Weaver, 1970; Meade and Jeanloz, 1988; and Uchida *et al.*, 1996; 2004) have found much higher yield strength compared with that measured in single crystals. Typically, single crystal deformation is accommodated by a single system mode, while in aggregates, stopping of dislocations at grain boundaries rapidly induces back stresses and forces the activity of multiple slip systems. This results in tangling of dislocations and rapid hardening caused by an increase in defect density. This mechanism is not well captured by current full crystal plasticity finite element models (Amodeo *et al.*, 2016). As such, the plastic behavior of polycrystalline periclase under confining pressure remains a topic of general interest. Here, we report new results on texture and lattice strain evolution in polycrystalline periclase deformed in the Deformation-DIA (D-DIA) up to 5.4 GPa at ambient temperature. We compare the experimental texture and lattice strain evolution with results of Elasto-Viscoplastic Self-Consistent (EVPSC) simulations (Wang *et al.*, 2010a) in order to obtain information about active plastic deformation mechanisms as well as strength and hardening parameters under the experimental conditions.

II. EXPERIMENT DETAILS

In this study, deformation of periclase was performed in the D-DIA at the European Synchrotron Radiation Facility (ESRF) beamline ID06 (Guignard and Crichton, 2015). The x-rays pass through the anvil gap and diffraction images are recorded on a linear x-ray detector covering an approximate 10° angle in 2θ. The linear detector is rotated perpendicular to the beam, allowing for full 360° azimuthal coverage. The sample to detector distance was 2057 mm with an x-ray wavelength of 0.22542 Å. Detector geometry was calibrated using a LaB_6 standard. Sample dimensions and strains were monitored using *in-situ* x-ray radiographs, as is typically performed in D-DIA experiments (e.g., Wang *et al.*, 2010b). A typical diffraction pattern is shown in Fig. S1 (supplementary material).

The starting material, a commercial MgO powder from Alfa Aesar (part #14684, 99.95% purity, 325 mesh), was loaded in a cubic cell similar to that outlined in Guignard and Crichton (2015). The dimensions of the sample are 3 mm height × 2 mm diameter. The D-DIA was closed and pressure was increased up to 4 GPa. The sample was then sintered at 1000 °C over 90 min in order to generate a homogenous microstructure. After sintering, the pressure was 2.2 GPa. We then imposed a deformation by axial compression to the sample by advancing the vertical anvils toward the sample while retracting the horizontal anvils. The overall duration of the deformation experiment was 264 min to a total macroscopic strain ε_{33} of ~37%. We impose an initial strain rate of 9.52×10^{-6}/s during which the hydrostatic pressure stabilizes. Following this, the sample was deformed at two successive strain rates of, 2.26×10^{-5}/s and 4.30×10^{-5}/s (Fig. 1), with the aim of evaluating the stress exponent of the rate sensitive power law equation.

The microstructure of the run-product was analyzed using electron microscopy at the Centre Commun de Microscopie of the Université de Lille (Fig. 2). Thin sections were extracted using a scanning electronic microscope (SEM) equipped with a focused ion beam (FIB) column [Fig. 2(a)]. A Philips CM30 transmission electron microscope (TEM), operating at 300 kV, was then used to investigate the sample microstructures. The observed image and diffraction demonstrate the homogeneous microstructure at the 10 μm scale [Fig. 2(b)]. At a finer scale, the diffraction image is spotty and shows individual grains [Fig. 2(c)]. TEM images were complemented by a map of crystal orientations in a second JEOL JSM-8000F LV SEM equipped with a system for transmission Kikuchi diffraction (TKD) allowing for orientation mapping of small grains within a thin sample. Representative higher resolution TEM image [Fig. 2(d)] and TKD-SEM orientation mapping of the same region [Fig. 2(e)] demonstrate that grain sizes range from ~10 nm to ~600 nm. The grains are often elongated perpendicular to the compression direction. Defect concentration is high and heterogeneous, indicating intense deformation by dislocation-induced plasticity.

III. EXPERIMENT DATA ANALYSIS

A. Stress and lattice strain

Due to the axial compression geometry in the D-DIA and the axial symmetry of the initial texture, the average

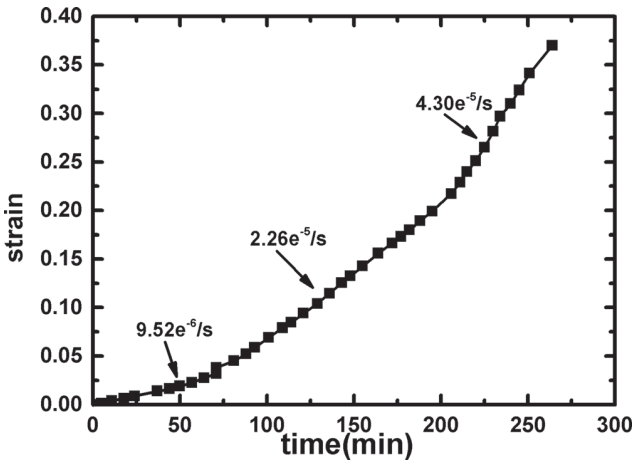

FIG. 1. Macroscopic strain ε_{33} evolution with time, as deduced from the x-ray radiographs of the sample.

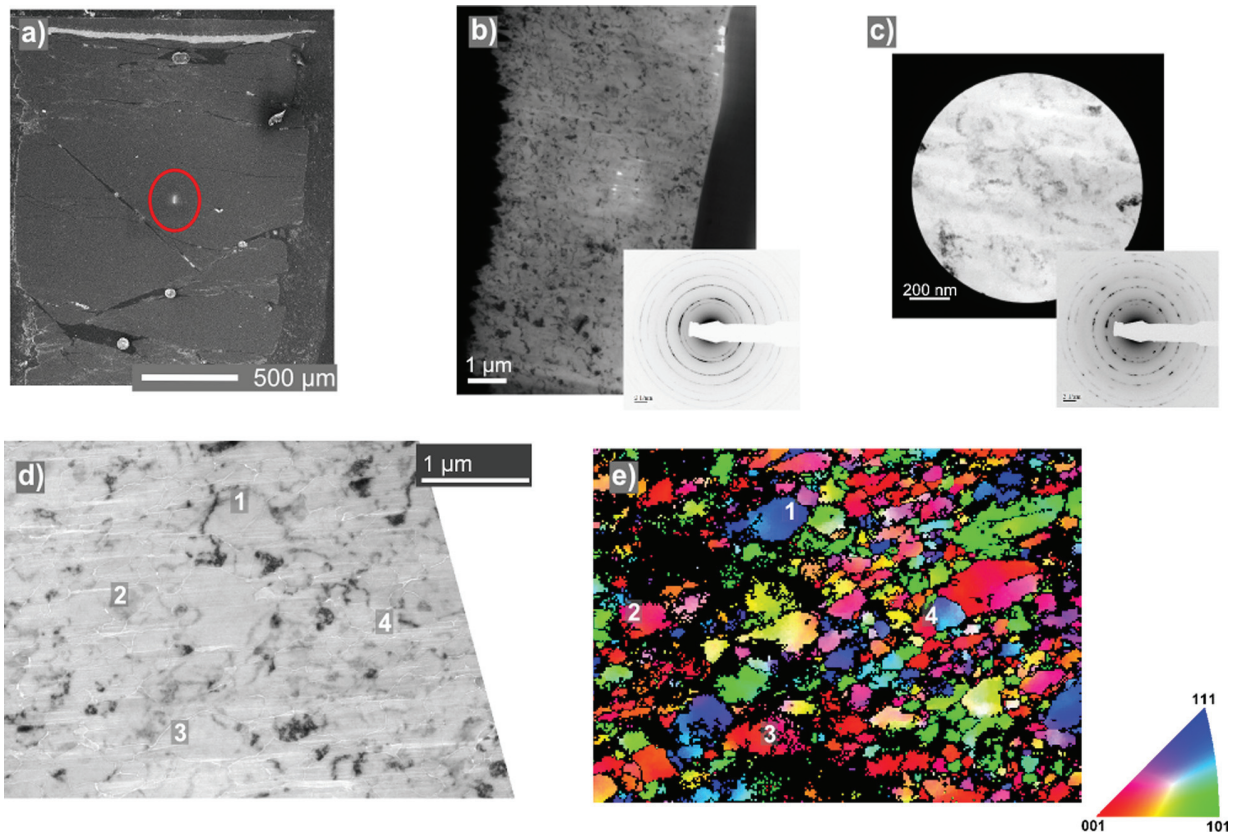

FIG. 2. SEM and TEM images of the recovered sample. (a) SEM image of the whole recovered sample. The region with a FIB section extracted for TEM and SEM-TKD is highlighted with a circle. Macroscopic compression direction is vertical. (b) Overview TEM image of the FIB section with the corresponding diffraction image in the inset. (c) TEM image at a finer scale and corresponding diffraction image. (d) Representative higher resolution TEM image. (e) TKD-SEM orientation mapping of the same region as (d). Grains are colored according to their orientation relative to the compression direction. Number 1–4 in (d) and (e) indicate grains that can be seen in both images.

sample stress tensor can be decomposed into hydrostatic and deviatoric components as

$$\sigma = \begin{bmatrix} \sigma_1 & 0 & 0 \\ 0 & \sigma_1 & 0 \\ 0 & 0 & \sigma_3 \end{bmatrix} = \begin{bmatrix} \sigma_p & 0 & 0 \\ 0 & \sigma_p & 0 \\ 0 & 0 & \sigma_p \end{bmatrix} + \begin{bmatrix} -\frac{t}{3} & 0 & 0 \\ 0 & -\frac{t}{3} & 0 \\ 0 & 0 & \frac{2t}{3} \end{bmatrix}, \quad (1)$$

where $\sigma_p = \frac{2\sigma_1+\sigma_3}{3}$ is the hydrostatic stress and $t = \sigma_3 - \sigma_1$. The value of $\boldsymbol{t}$ can be used to infer the flow strength of the material. Under a deviatoric stress superimposed on the hydrostatic pressure, the measured d-spacing varies as a function of the angle between the diffraction plane normal and the compression axis, χ. The measured d-spacing can be expressed as (Singh, 1993)

$$d_m(hkl) = d_p(hkl)\left[1 + \left(1 - 3\cos^2\chi\right)Q(hkl)\right], \quad (2)$$

where (hkl) are the Miller indices indicating the diffraction plane, d_m is the experimentally measured d-spacing, and d_p is the d-spacing under hydrostatic stress σ_p. $Q(hkl)$ describes the shift in d_m from d_p for diffraction plane (hkl) due to deviatoric stress. When $Q(hkl)$ is 0, the polycrystals are under pure hydrostatic stress. $Q(hkl)$ and d_p can be obtained by fitting d_m and χ in Eq. (2) from the experimental data. The expression in Eq. (2) was derived from an elastic model that does not account for plastic relaxation. Experiments have shown, however, that it remains an efficient method for expressing the effect of deviatoric stress and comparing the experimental results to numerical models in the presence of plastic relaxation (Merkel *et al.*, 2009; 2012). A typical fit of the diffraction data to Eq. (2) is shown in Fig. S2 (supplementary material).

The hydrostatic stress can be calculated from d_p through the use of an appropriate Equation of State (EoS). Using the measured d_p, we calculate the unit cell volume of the material and use a 3rd order Birch-Murnaghan Eos (Birch, 1947)

$$P(V) = \frac{3}{2}K_0\left[\left(\frac{V_0}{V}\right)^{\frac{7}{3}} - \left(\frac{V_0}{V}\right)^{\frac{5}{3}}\right] \times \left\{1 + \frac{3}{4}\left(K_0' - 4\right)\left[\left(\frac{V_0}{V}\right)^{\frac{2}{3}} - 1\right]\right\}, \quad (3)$$

where V_0, K_0, and K_0' are the unit cell volume, bulk modulus, and pressure derivative of the bulk modulus of periclase at room pressure, respectively, and V is the measured unit cell volume. To determine pressure in periclase, we use the EoS

parameters of Zha *et al.*, (2000). In this study, hydrostatic stress and Q-factors are calculated using the POLYDEFIX package (Merkel and Hilairet, 2015). A first estimate of the differential stress $\boldsymbol{t}$ is given by the empirical relation (Singh *et al.*, 1998)

$$t(hkl) = 6GQ(hkl), \tag{4}$$

where G is the shear modulus of the aggregate. For this study, we use the single crystal elastic properties for periclase from Zha *et al.*, (2000). Note, however, that an estimate of $\boldsymbol{t}$ based on elasto-plastic models (see later) is a more physically grounded method of determining $\boldsymbol{t}$ (e.g., Li *et al.*, 2004).

B. Texture

Synchrotron diffraction images are analyzed using the Rietveld method as implemented in the Materials Analysis Using Diffraction (MAUD) software package (Lutterotti *et al.*, 1997). Refinement generally follows the procedure for high pressure data as outlined in Wenk *et al.*, (2014) with the addition that an intensity correction is used to account for the D-DIA anvil shadows (Miyagi *et al.*, 2008). Systematic variations in intensity along diffraction rings indicate the existence of texture. The Orientation Distribution Function (ODF) is computed using the Extended Williams, Imhof, Matthies, and Vinel (E-WIMV) algorithm which is similar to the WIMV method (Matthies and Vinel, 1982). The ODF is then exported from MAUD and smoothed with a 7.5° Gauss filter using the program Beartex (Wenk *et al.*, 1998). In the case of axial compression, cylindrical symmetry about the compression axis can be assumed and textures are compactly represented with an Inverse Pole Figure (IPF) of the compression direction. IPFs show the relation between the compression direction and the crystal axes. Pole densities are expressed in multiples of random distribution (m.r.d.), where an m.r.d. of 1 corresponds to a random distribution, and in the case of a perfectly oriented sample or a single crystal, the m.r.d. would be equal to infinity for the orientation of the crystal and 0 elsewhere. A typical refinement is shown in Fig. S3 (supplementary material).

C. Experimental results

After the quasi-hydrostatic loading and sintering stage, the pressure was 2.2 GPa. Upon deforming the sample with the differential rams, the pressure reached ~5 GPa within a few % strain, increased up to 5.4 GPa for 20.4% strain, and then remained constant (Fig. 3). Q-factors increased elastically up to a strain of ~2.4%. Past this point, there was a pronounced drop of Q(200), which decreased from a value of 0.006 to 0.004. There were also minor decreases in Q(111) and Q(220). After the strain reached 7%, Q-factors increased steadily, likely due to strain hardening. When the strain rate was doubled at around 20.4% strain, there was no large jump in Q-factors. Since Q-factors were indicative of a macroscopic stress on the sample, this suggested a relatively large stress exponent (Fig. 4). Indeed, a sample in dislocation creep should deform according to

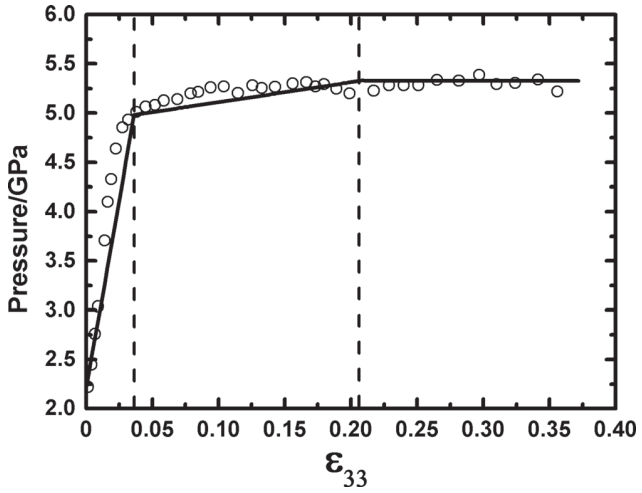

FIG. 3. Hydrostatic stress evolution with macroscopic strain ε_{33}. Circles indicate the experiment data. The solid line is the path followed by the optimized EVPSC simulation. The dashed lines indicate strain rate changes during the experiment.

$$\dot{\varepsilon} = A(P,T)t^n, \tag{5}$$

where $\boldsymbol{A}(\boldsymbol{P},\boldsymbol{T})$ is a factor depending on $\boldsymbol{P}$ and $\boldsymbol{T}$, $\boldsymbol{t}$ the differential stress, and $\boldsymbol{n}$ the stress exponent. For $\boldsymbol{t}$ to be weakly dependent on the strain rate, $\boldsymbol{n}$ must be large. A stress exponent of $\boldsymbol{n} = 30$ was used in EVPSC simulations of experiment data.

Four IPFs were selected from the whole deformation process at various strains in order to demonstrate the evolution of the experimental texture (Fig. 5). At the start of deformation, the texture was essentially random with a maximum m.r.d. of 1.1. When the macroscopic strain was below ~4%, the hydrostatic stress increase was rapid (Fig. 3). Texture development was slow while the measured lattice strains were still increasing (Figs. 4 and 5). With increasing strain, periclase gradually developed a strong (100) texture with a fiber toward (110), reaching a maximum m.r.d. of 4.0 at ~37% strain.

IV. EVPSC SIMULATION

EVPSC (Wang *et al.*, 2010a) is an effective medium self-consistent method, which treats each grain in

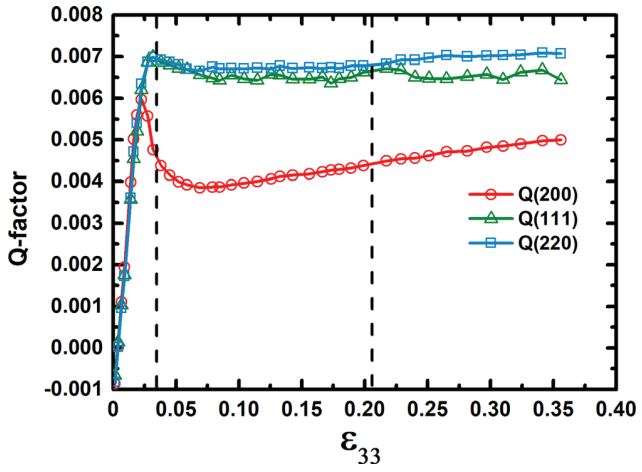

FIG. 4. Q-factors evolution with macroscopic strain ε_{33} as measured in the experiment.

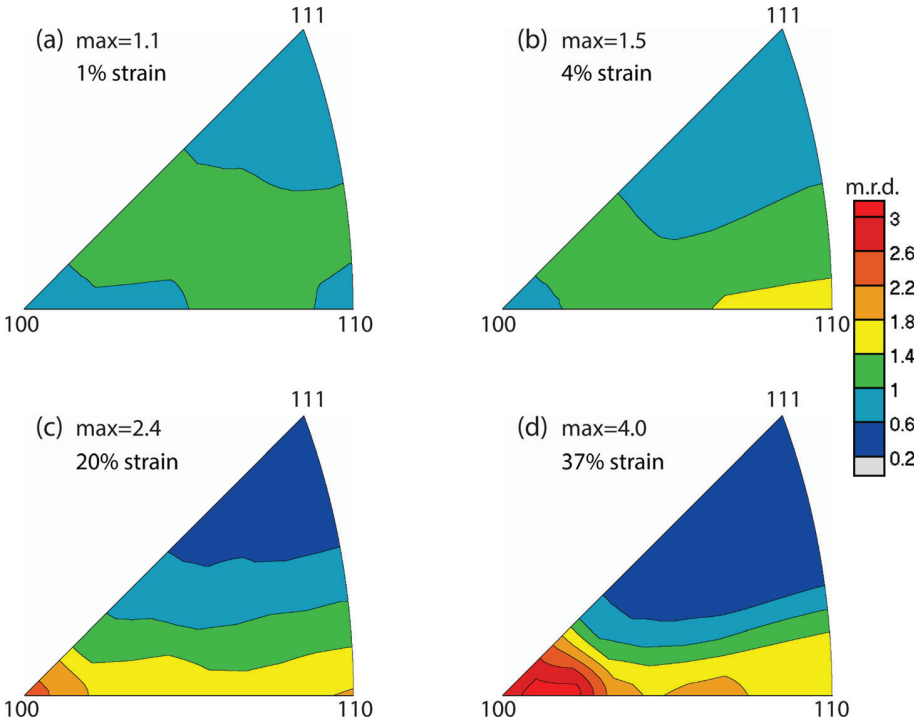

FIG. 5. Experiment texture evolution with macroscopic strain ε_{33}. 1% strain (a); 4% strain (b); 20% strain (c); 37% strain (d). Equal area projection. Linear scale expressed in m.r.d.

polycrystals as an inclusion in a homogeneous but anisotropic medium. The properties of the medium are determined by the average of all the inclusions. At each deformation step, the inclusion and medium interact and the macroscopic elasto-plastic properties are updated iteratively until the average strain and stress of all the inclusions equal the macroscopic strain and stress. In this study, a step increment of 0.002 strain is used. The advantage of EVPSC as compared with other self-consistent methods like the Elasto-Plastic Self-Consistent (EPSC) code (Turner and Tomé, 1994) and Visco-Plastic Self-Consistent (VPSC) code (Lebensohn and Tomé, 1994) is that EVPSC can account for both the elastic and viscoplastic behavior of the material. Calculations account for elastic stress, grain rotation, and relaxation due to plasticity, and strain rate dependence of the plastic behavior. In each grain, the EVPSC code accounts for elastic strain and orientation, which can be used to reconstruct both lattice strains and textures, as one would measure in an experiment.

For EVPSC simulations, one needs to impose the deformation rate matrix applied to the overall sample. In our case, we optimized the deformation rates by accounting for the measured macroscopic axial strains (Fig. 1) and the evolution of hydrostatic stress (Fig. 3). Due to the shape of the anvil gap in D-DIA experiments, only the strain and strain rate in the compression direction ($\dot{\varepsilon}_{33}$) can be measured. The volume change is the trace of the deformation matrix and can be calculated from Eq. (3). Due to the geometry of axial compression in the D-DIA, $\dot{\varepsilon}_{11} = \dot{\varepsilon}_{22}$, and knowing the evolution of the hydrostatic stress vs. macroscopic axial strain, all components of the deformation matrix can be determined (Fig. 6). A good fit is obtained when the evolution of pressure vs. ε_{33} is the same as measured in the experiment.

In EVPSC, the rate-sensitive constitutive law for plastic deformation is given by

$$\dot{\varepsilon}_{ij} = \dot{\gamma}_0 \sum_s m^s_{ij} \left\{ \frac{m^s_{kl}\sigma_{kl}}{\tau^s} \right\}^n, \tag{6}$$

where $\dot{\gamma}_0$ is the reference shear strain rate, τ^s is the resolved shear stress of a slip system s at the reference strain rate, m^s_{kl} is the symmetric Schmid factor for the slip system s, n is an empirical stress exponent for a given slip system. σ_{kl} is the local stress tensor. Strain hardening/softening of each plastic mechanism is represented using an extended Voce hardening law (Tomé *et al.*, 1984)

$$.\hat{\tau}^s = \tau^s_0 + \left(\tau^s_1 + \theta^s_1 \Gamma\right)\left(1 - \exp\left(-\Gamma\left|\frac{\theta^s_0}{\tau^s_1}\right|\right)\right), \tag{7}$$

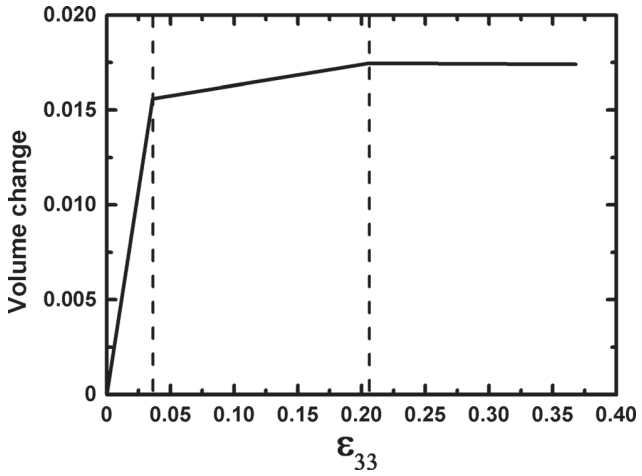

FIG. 6. Sample volume evolution with axial strain ε_{33} in the EVPSC optimization. The dashed lines indicate strain rate changes during the simulation. Volume is chosen to match the change of hydrostatic stress in the experiment. Compression strain and volume reduction is positive.

where $\boldsymbol{\Gamma}$ is the accumulated shear strain in the grain, $\tau_0^s, \theta_0^s, \theta_1^s, (\tau_0^s + \tau_1^s)$ are the initial critical resolved shear stress (CRSS), initial hardening rate, asymptotic hardening rate, and back-extrapolated CRSS for the slip system s. Under the self-consistent scheme, the rate-sensitive equation needs to be linearized. There are several homogenization schemes possible, namely, secant, affine, and tangent, which represent increasing medium compliance vis-a-vis the interaction with the grain (e.g., Castelnau *et al.*, 2008). The tangent assumption allows more heterogeneity of strain from grain to grain and tends to predict a uniform stress state for large values of n. The secant assumptions are stiff and tend to predict a uniform strain-rate from grain to grain when n is large. On the other hand, the affine model is intermediate between secant and tangent bounds, and better suited when the exponent n is large [see Figs. 1(a) and 1(b) in Lebensohn *et al.*, 2007]. The absolute values and the ratios of CRSS of different slip systems affect their plastic response and activity. In addition to CRSS values and work hardening/softening, the initial grain shape and the linearization assumption in EVPSC can also be chosen and affects the resulting lattice strain and texture evolution.

A. Lattice strain and texture simulations

In this study, three slip modes, $\{110\}\langle 1\bar{1}0\rangle$, $\{100\}\langle 011\rangle$, and $\{111\}\langle 1\bar{1}0\rangle$ are assumed in periclase. By modifying the CRSS, strain hardening parameters, and exponent n of the rate-sensitive law for different slip systems, Q-factors and texture evolution are simulated with increasing macroscopic strain.

1. Single active slip system test

In order to understand how the slip systems affect Q-factors and texture evolution, only a single dominant slip mode is activated in the following EVPSC simulations. The deformation process follows the solid lines in Fig. 6 with the same strain rate as in the experiment. For simplicity, only the initial CRSS and the initial grain shape are treated as variables here. The initial grain shape is represented using the ratio of three principal ellipsoid axes in the sample system. In these simulations, initial grain shapes of (1.0, 1.0, 1.0) and (1.0, 1.0, 0.6) are chosen. The former indicate spherical grains at the start of the simulation, while the latter (1.0, 1.0, 0.6) indicate an oblate grain in the compression direction. The pressure dependence of single crystal elastic constants reported by Zha *et al.* (2000) is used to calculate the variation of MgO elastic constants with increasing pressure. By modifying the initial CRSS of the three different slip modes (Table I), we can force each slip mode to accommodate all strain. Imposing different slip system activities results in a different ordering of the Q-factors. The ordering of the Q-factors for dominant slip on $\{110\}\langle 1\bar{1}0\rangle$ [Fig. 7(a)] is most similar to the experimental results (Fig. 4). Changes in the initial grain shape result in only slight changes in Q-factors. When the dominant slip system is $\{100\}\langle 011\rangle$ or $\{111\}\langle 1\bar{1}0\rangle$, the effect of initial grain shape on Q-factors is negligible, but is slightly more pronounced when the $\{110\}\langle 1\bar{1}0\rangle$ slip system is dominant [Figs. 7(a) and 7(d)].

TABLE I. CRSS for different slip systems in one slip system EVPSC test.[a]

Slip system	CRSS (GPa)[b]	CRSS (GPa)[c]	CRSS (GPa)[d]
$\{110\}\langle 1\bar{1}0\rangle$	2.0	15.0	15.0
$\{100\}\langle 011\rangle$	15.0	2.0	15.0
$\{111\}\langle 1\text{–}10\rangle$	15.0	15.0	2.0

[a]Tangent assumption, exponent $n = 10$.
[b]CRSS values used for activating only $\{110\}\langle 1\bar{1}0\rangle$.
[c]CRSS values used for activating only $\{100\}\langle 011\rangle$.
[d]CRSS values used for activating only $\{111\}\langle 1\text{–}10\rangle$.

Thus, in addition to strain hardening/softening, initial grain shape can have a small effect on the simulated Q-factors.

Different dominant slip systems lead to different and characteristic textures (Fig. 8). When only the $\{110\}\langle 1\bar{1}0\rangle$ slip system is active, a (100) texture component develops. The experimental compression texture of periclase closely resembles this simulation. Textures for $\{100\}\langle 011\rangle$ slip are characterized by a (110) texture with a fiber toward (100). Slip on $\{111\}\langle 1\bar{1}0\rangle$ results in a strong texture component at (110). In contrast to the Q-factor evolution, the initial grain shape does have a significant effect on the texture evolution. In simulations with initially flat grains, the texture tends to evolve more quickly and is stronger at a given strain (Fig. 8). This effect is pronounced for dominant slip on $\{110\}\langle 1\bar{1}0\rangle$ [Figs. 8(a) and 8(b)]. For slip on $\{110\}\langle 1\bar{1}0\rangle$, this is likely due to the fact that for this slip mode, each slip system has a symmetric variant with an identical Schmid factor but with an equal and opposite rotation [e.g., $(110)[\bar{1}10]$ and $(\bar{1}10)[110]$]. Thus, for $\{110\}\langle 1\bar{1}0\rangle$ slip, the spins of the symmetric variants cancel each other's rotation. This results in slow texture evolution until strain is large enough to cause enough flattening of the grains that the rotation of the ellipsoid adds to the crystallographic rotation (Wenk *et al.*, 1989). By starting the simulation with initially flat grains, the texture evolution can proceed more rapidly.

2. D-DIA experiment simulation

Based on the order of the Q-factors and the texture evolution, we conclude that $\{110\}\langle 1\bar{1}0\rangle$ is dominant in our experiment. Consequently, the CRSS of $\{110\}\langle 1\bar{1}0\rangle$ slip system is assigned to be small compared with $\{100\}\langle 011\rangle$. Theoretical calculations indicate that it is difficult to activate $\{111\}\langle 1\bar{1}0\rangle$ slip at a low temperature (Amodeo *et al.*, 2016). Thus, in the following simulations, it is assumed that $\{111\}\langle 1\bar{1}0\rangle$ is not activated and so it is assigned a relatively high CRSS to suppress its activity. For the best fit simulation, an initial grain shape (1.0, 1.0, 0.8) is used. A parabolic shape Voce hardening gives a rapid drop and then increase of Q-factors as is observed in the experiment (Fig. 4). In addition to the "best fit" model, we performed simulations to match the high Q-factors (transient, without strain softening) as well as the low Q-factors (quasi-steady state, back extrapolation of strain hardening). A linear Voce hardening is used to simulate both the high and low Q-factors (Fig. 9). Optimized parameters for different scenarios are shown in

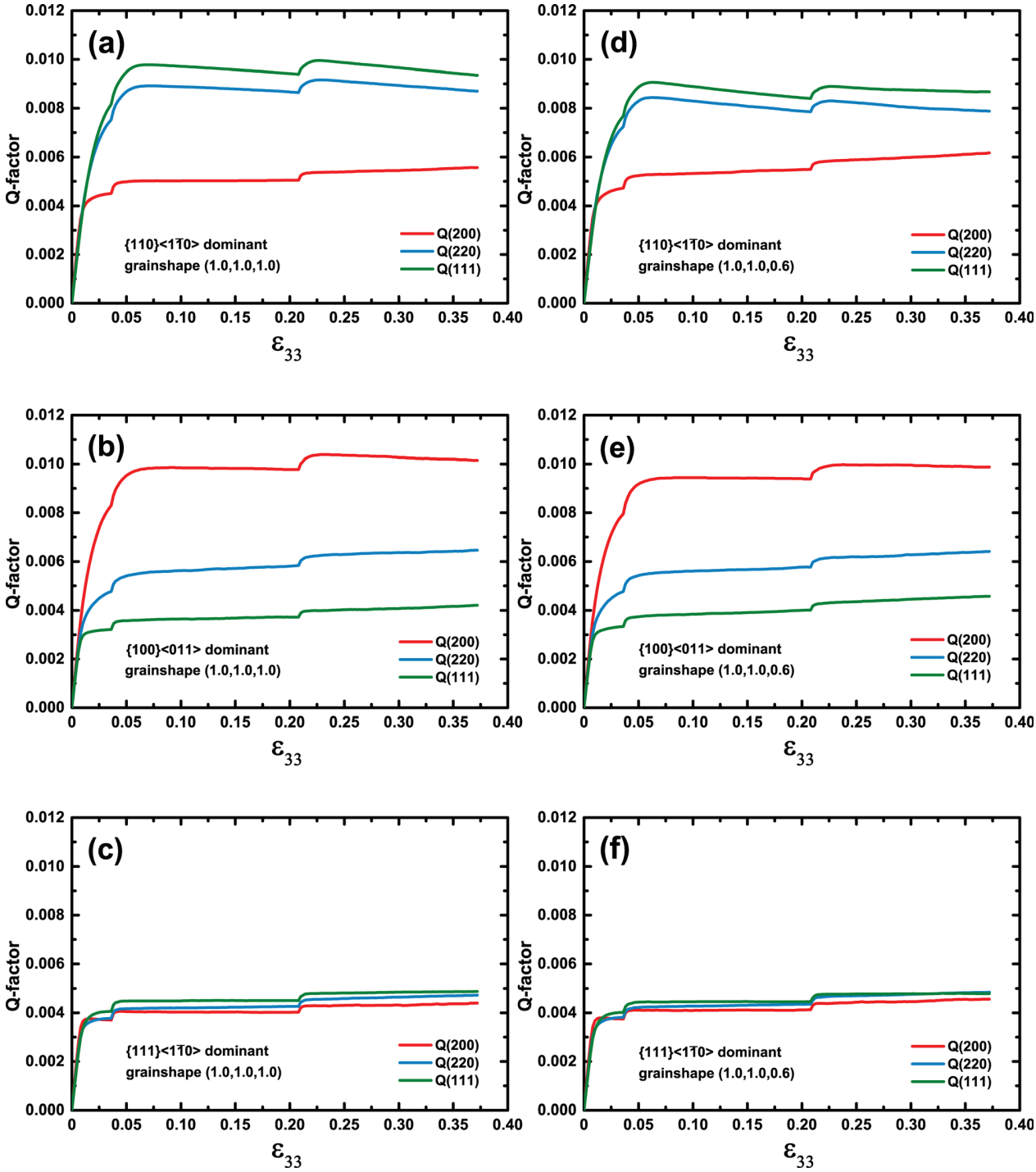

FIG. 7. Q-factor evolution with macroscopic strain ε_{33} for single active slip mode, predicted using the tangent approximation. Initial grain shape of (1.0, 1.0, 1.0) [(a), (b), (c)] and (1.0, 1.0, 0.6) [(d), (e), (f)]. Simulations with dominant slip on $\{110\}\langle 1\bar{1}0\rangle$ [(a), (d)]; $\{100\}\langle 011\rangle$ [(b), (e)]; and $\{111\}\langle 1\bar{1}0\rangle$ [(c), (f)].

Table II. It is worthy to note that the CRSS used in EVPSC corresponds to polycrystals, which is much higher than the single crystal CRSS due to grain–grain interactions and boundary effects. In EVPSC, this effect is represented by the interaction between the Homogenous Effective Medium (HEM) and inclusions. Here, we test the so-called tangent and affine linearization assumption to determine the effect on Q-factors evolution and texture development.

For the low Q-factors simulation, the best fit is achieved with the affine assumption [Figs. 10(c) and 10(d)]. The CRSS of the $\{110\}\langle 1\bar{1}0\rangle$ slip system starts at 1.2 GPa and then increases by a linear strain hardening with a slope of 0.4 (Fig. 9). The CRSS of the $\{100\}\langle 011\rangle$ slip system starts at 3.2 GPa. A strain hardening/softening effect is not obvious for the $\{100\}\langle 011\rangle$ slip system. For the high Q-factors simulation, a better fit is obtained when using the tangent

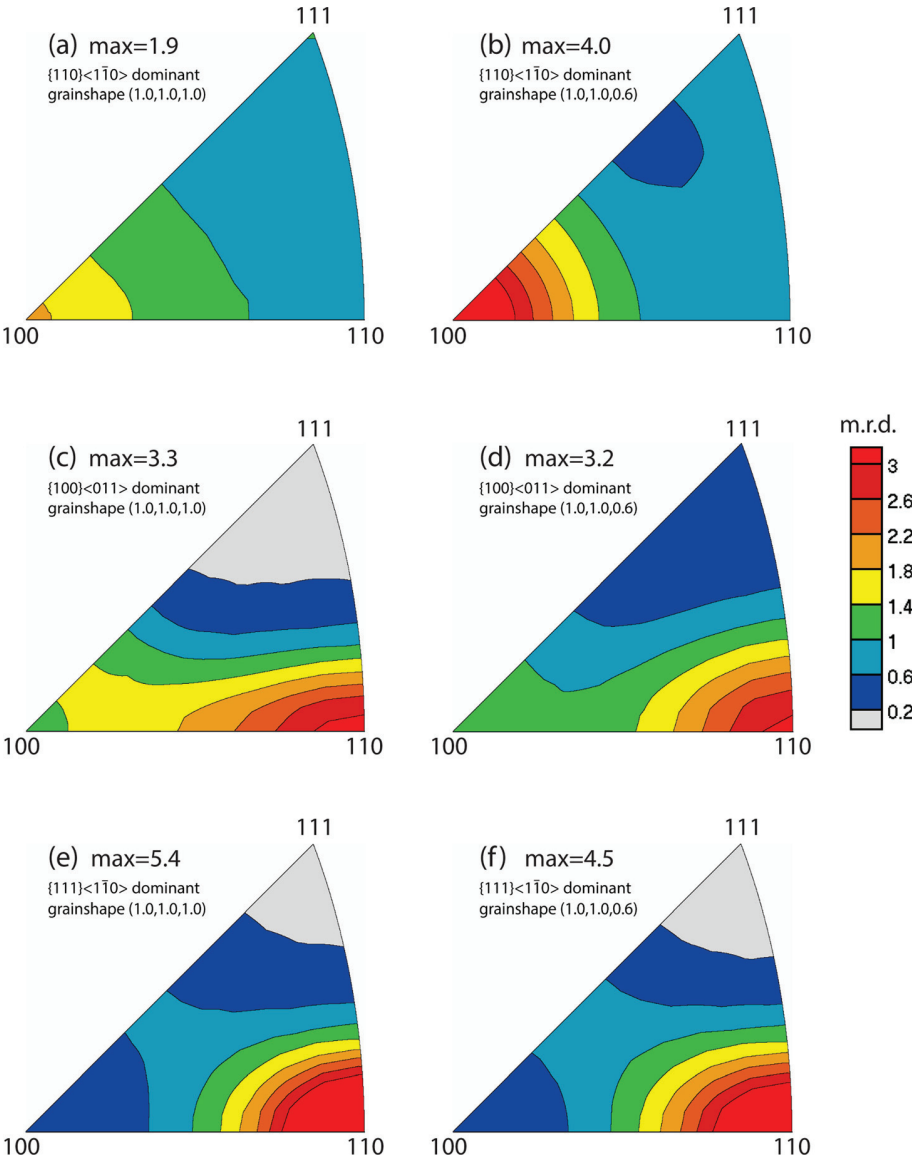

FIG. 8. Inverse pole figure (equal area projection) of the simulated sample textures after 37% axial strain predicted using the tangent approximation, with round grain shapes [(a), (c), and (e)] and flat grains [(b), (d), and (f)]. Dominant slip on $\{110\}\langle 1\bar{1}0\rangle$ [(a) and (b)], $\{100\}\langle 011\rangle$ [(c) and (d)] and $\{111\}\langle 1\bar{1}0\rangle$ [(e) and (f)].

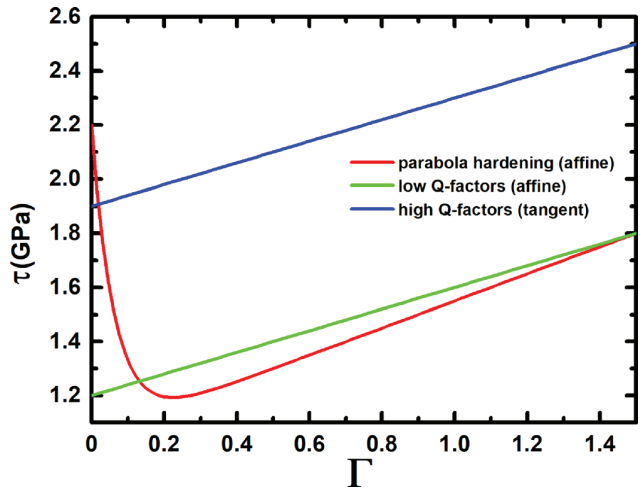

FIG. 9. Optimized Voce strain softening/hardening curves of $\{110\}\langle 1\bar{1}0\rangle$ in simulations accounting for the full variation of {200} lattice strains (red line), high values of lattice strains (blue line), and quasi-steady state lattice strains (green line).

assumption. The CRSS of $\{110\}\langle 1\bar{1}0\rangle$ starts at 1.9 GPa and then increases with a slope of 0.2 (Fig. 9). The CRSS of the $\{100\}\langle 011\rangle$ slip system must be high enough to suppress this slip system in order to obtain a good fit. A characteristic (100) texture is developed in all scenarios (Fig. 11). The texture is stronger and more focused in (100) for the high Q-factors simulation (tangent) and weaker in the low Q-factors simulation

TABLE II. Parameter used in EVPSC modeling.

	Slip system	τ_0 (GPa)	τ_1 (GPa)	θ_0 (GPa)	θ_1 (GPa)	n
High Q-factor (tangent)	$\{110\}\langle 1\bar{1}0\rangle$	1.9	0	0.2	0.2	30
	$\{100\}\langle 011\rangle$	10.0	0	0	0	30
	$\{111\}\langle 1\bar{1}0\rangle$	15.0	0	0	0	30
Low Q-factor (affine)	$\{110\}\langle 1\bar{1}0\rangle$	1.2	0	0.4	0.4	30
	$\{100\}\langle 011\rangle$	3.2	0	−0.2	−0.2	30
	$\{111\}\langle 1\bar{1}0\rangle$	15.0	0	0	0	30
Parabolic hardening (affine)	$\{110\}\langle 1\bar{1}0\rangle$	2.2	−1.2	−18.0	0.65	30
	$\{100\}\langle 011\rangle$	3.1	0	−0.1	−0.1	30
	$\{111\}\langle 1\bar{1}0\rangle$	15.0	0	0	0	30

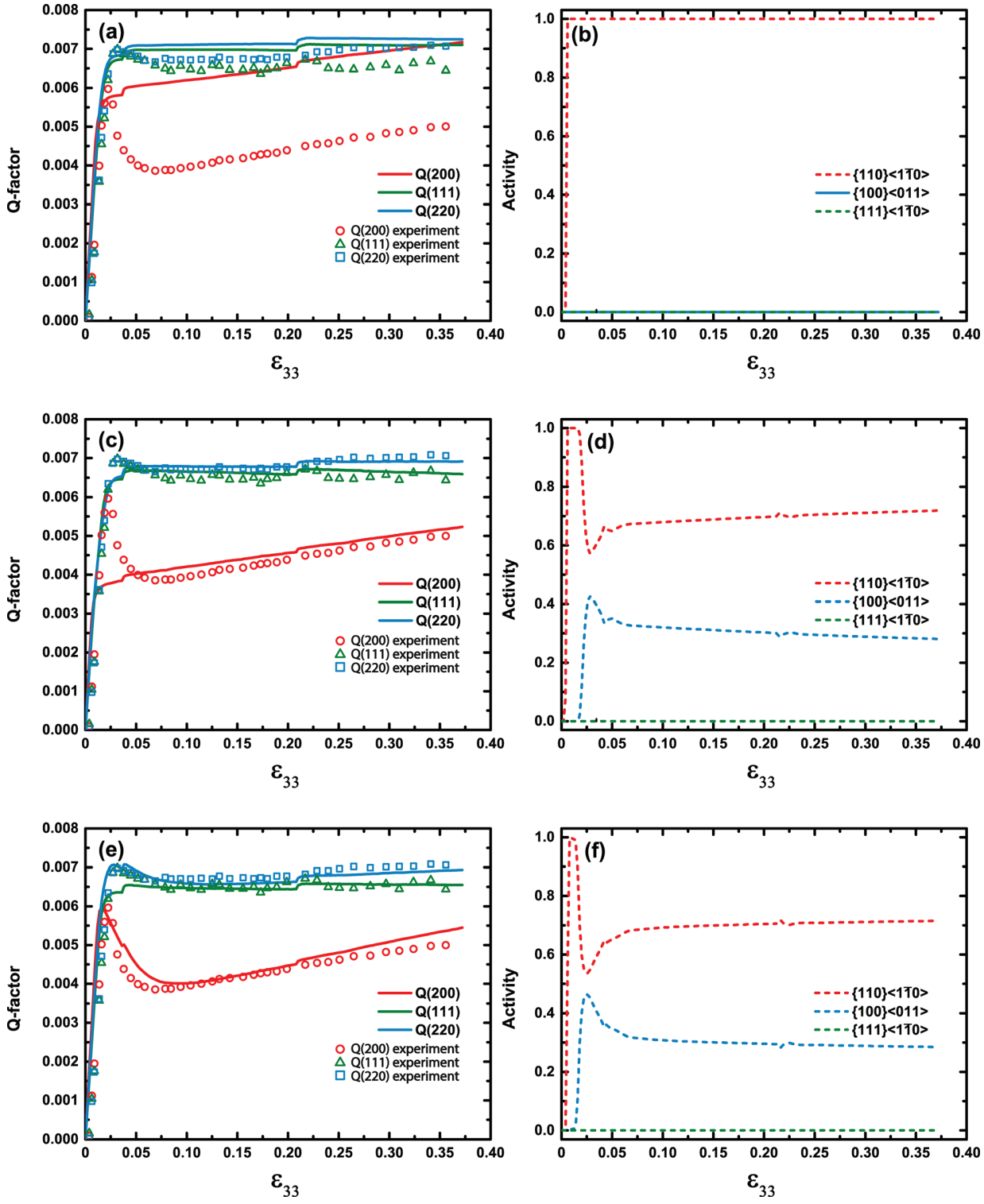

FIG. 10. EVPSC simulation of Q-factors and slip system activities. Open shape represents experiment Q-factors. High Q-factors (tangent) (a) and (b), low Q-factors (affine) (c) and (d), and parabolic shape strain hardening (affine) (e) and (f).

(affine). The uniaxial stress t evolution with macroscopic strain calculated for different scenarios in EVPSC is similar to each other. The value of t for the parabolic hardening is very close to the average of $t(hkl)$ deduced from empirical equation (4) (Fig. 12). The supplementary material (Figs. S4–S7) contains additional modeling predictions for varying initial grain shape and linearization assumption scheme.

V. DISCUSSION

A. Lattice strains relaxation after yielding: Effect of pinning due to impurities?

The evolution of Q-factors with deformation is somewhat unexpected, particularly in the case of Q(200) for which a drop is observed after a few percent deformation.

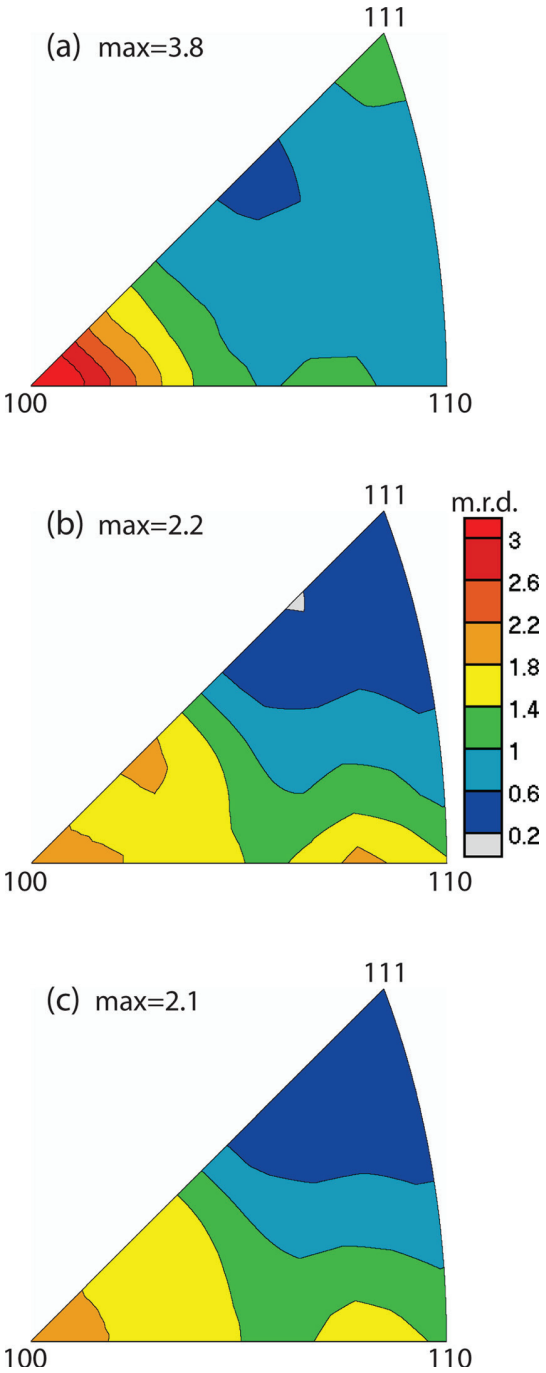

FIG. 11. EVPSC simulation of texture. High Q-factors (tangent) (a); low Q-factors (affine) (b); and parabolic strain hardening (affine) (c).

This seems to indicate that after initial yielding, dislocations become more mobile, thus reducing the flow strength. An increase in grain size upon deformation can reduce the flow strength. However, in this experiment, periclase was deformed at room temperature, and thus, recrystallization is unlikely to occur. This is confirmed with the electron microscopy observations of the run-product that indicate a typical grain size on the order of ~200 nm (Fig. 2).

Another possibility is that the initial peak in Q-factors is due to pinning of dislocations by impurities. A similar behavior has been found in a previous experiment (Paterson and Weaver, 1970), which may be caused by Li and F impurities. Indeed, upon recovery and sectioning of the sample, it was observed that the sample is darker than the starting material. This is likely due to carbon contamination (Freund, 1986), presumably from the graphite heater used for *in-situ* sintering of the sample. Pinning effectively increases the CRSS, which causes the Q-factors to reach the peak value. When the local stress is high enough, dislocations unpin from the carbon solute cloud. The carbon will not have enough mobility at room temperature to "follow" the dislocation motion. The CRSS needed for dislocation motion will drop rapidly and large deviatoric lattice strains due to pinning are relaxed. The Q-factors decrease to a value close to that of a sample with no pinning. Hence we suspect that the lowest Q-factor values represent the true flow curve of polycrystalline periclase at 300 K while the maximum values represent deformation with the effects of pinning (Fig. 4).

B. Effect of the linearization assumption of the self-consistent scheme

In EVPSC, the linearization scheme has an influence on the simulation results. The tangent assumption allows more strain heterogeneity between grains, which results in lower Q(111) and Q(220) compared with other assumptions. In the simulation using the tangent method, when the CRSS of the $\{110\}\langle 1\bar{1}0\rangle$ slip system is low enough to fit the low Q(200) value ("steady-state" value), the maximum value of Q(220) and Q(111) are too low to fit the experiment (Fig. S6, supplementary material). Interestingly, the tangent approximation fits the experimental Q-factors well when fitting the high Q(200) value (transient maximum) [Figs. 10(a) and 10(b)].

On the other hand, the affine assumption does a better job when fitting low Q(200) values ("steady-state") (Figs. 10(c) and 10(d)]. For the high Q-factors value, the affine approximation results in a larger separation between Q(220) and Q(111) than is found in the experiment [Fig. S6(c), supplementary material]. Indeed, the affine model, where strain compatibility is prioritized, results in higher stresses and more activation of auxiliary slip systems. Q-factors predicted by the affine model (for "steady-state") are sensitive to the CRSS of the $\{100\}\langle 011\rangle$ slip system. Both $\{110\}\langle 1\bar{1}0\rangle$ and $\{100\}\langle 011\rangle$ need to be activated at ~70:30 ratio to have enough slip systems to accommodate macroscopic strain while achieving a satisfactory fit to the experimental "steady-state" Q-factors. Instead, when using a tangent model, more strain heterogeneity is permitted and the $\{110\}\langle 1\bar{1}0\rangle$ slip system can be fully activated while completely suppressing the $\{100\}\langle 011\rangle$ slip system.

The general features of the simulated texture are similar to the experiment (Fig. 5) when using affine; however, the intensity of the (100) texture component is much closer to the experiment when using tangent [Figs. 11(a) and 11(b)]. As shown in the single slip system simulations, a higher $\{110\}\langle 1\bar{1}0\rangle$ activity yields a more concentrated (100) component. For the simulation using the tangent approximation, the activity of $\{110\}\langle 1\bar{1}0\rangle$ is much higher than in those using an affine approximation, thus resulting in a stronger texture.

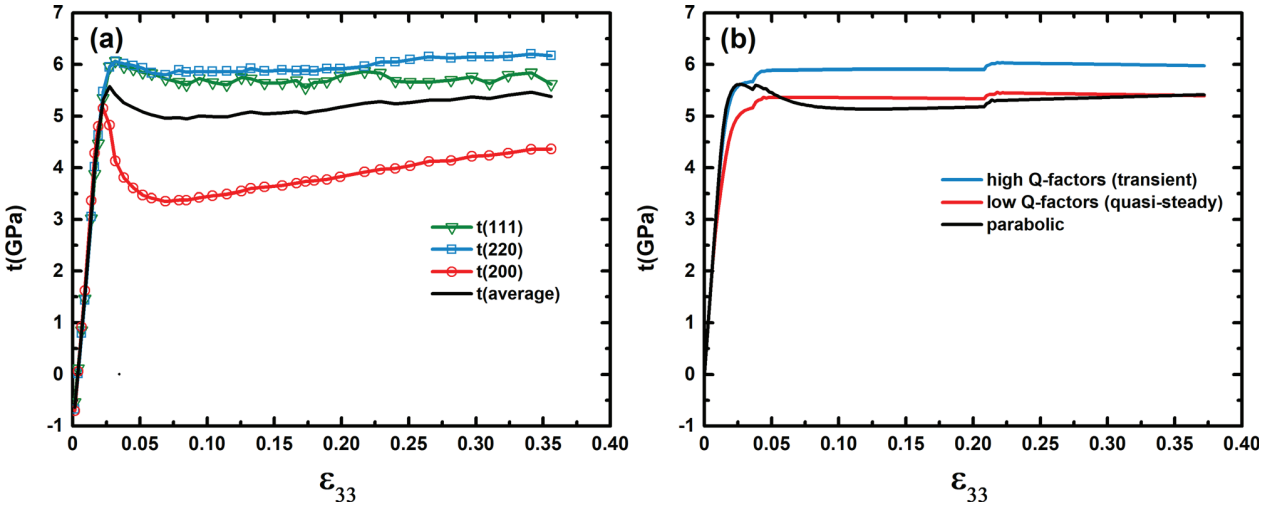

FIG. 12. Uniaxial stress t evolution with macroscopic strain ε_{33}. (a) Values calculated from the empirical equation (4) from the Q-factors measured for each lattice plane families; (b) values deduced from the EVPSC simulations (see details in the text).

C. Strength and plasticity of MgO at high pressure

According to Fig. 12, the calculated yield strength of MgO is around 5 GPa at 300 K at pressure around 5.4 GPa, which is about 2 or 3 GPa higher than the experimental results from Bridgman (1937), Kinsland and Bassett (1977), Weidner *et al.* (1994), and Uchida *et al.* (1996) but is in good agreement with Merkel *et al.* (2002) (Fig. 13). This could be due to grain size hardening described by the Hall-Petch effect (Hall, 1951 and Petch, 1953). Generally, smaller grain size results in higher yield strength. The average grain size of the MgO in this experiment is ~200 nm as estimated from SEM and TEM imaging of the run-product (Fig. 2). The yield strength we estimate is in good agreement with a room temperature, unconfined, *in-situ* TEM compression experiment on nanocrystalline MgO with a similar grain size, where yield stresses around 3–5 GPa were reported (Issa *et al.*, 2015). Therefore, at ambient T, pressure might have a much smaller effect than the grain size on MgO strength, in this pressure and grain size range.

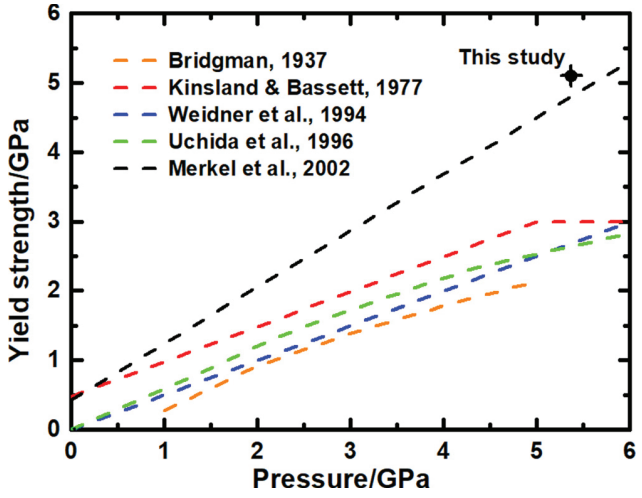

FIG. 13. Yield strength in this study compared with previous work performed under similar pressure. Bridgman (1937) (orange dash line); Uchida *et al.* (1996) (green dash line); Weidner *et al.* (1994) (blue dash line); Kinsland and Bassett (1977) (red dash line); Merkel *et al.* (2002) (black dash line).

Both our Q-factor evolution and texture development are consistent with dominant $\{110\}\langle 1\bar{1}0\rangle$ slip, similar to previous work on periclase in the Diamond Anvil Cell (DAC) (Merkel *et al.*, 2002). Interestingly, a previous D-DIA experiment to 8 GPa at ambient condition found a different Q-factor order than this study (Uchida *et al.*, 2004). This prior work found the largest Q factor to be Q(200) and the lowest to be Q(111), an order consistent with a high activity of the $\{100\}\langle 011\rangle$ slip system. It is possible that differences in deformation conditions or sample synthesis could account for differences in slip system activities. A pressure-induced slip system transition from $\{110\}\langle 1\bar{1}0\rangle$ to $\{100\}\langle 011\rangle$ between 20 and 50 GPa is suggested for single crystal periclase by both experiment and theoretical calculations (Girard *et al.*, 2012; Amodeo *et al.*, 2012; 2016). If a change in slip system occurs at high pressure, a shift in the texture maximum from (100) to (110) would be predicted. However, in previous DACs experiments on periclase and ferropericlase, this is not observed (Merkel *et al.*, 2002; Tommaseo *et al.*, 2006; and Marquardt and Miyagi, 2015). It is possible that in the DAC, there is insufficient strain after the slip system transition to erase the low pressure (100) texture.

In contrast to DAC experiments, a mixture of (100) and (110) compression texture for ferropericlase has been observed at 300 MPa and temperatures of 1200–1400 K (Stretton *et al.*, 2001). This is attributed to increased activity of $\{100\}\langle 011\rangle$ at high temperature, consistent with theoretical work by Amodeo *et al.* (2012; 2016) and experiments.(e.g., Copley and Pask, 1965 and Day and Stokes, 1966). These previous studies seem to indicate that $\{100\}\langle 011\rangle$ could become more active in periclase and ferropericlase both with higher pressure and with higher temperature. Thus, in the Earth's lower mantle, it is possible that $\{100\}\langle 011\rangle$ slip is dominant in ferropericlase as opposed to $\{110\}\langle 1\bar{1}0\rangle$, which has been widely assumed. In the future, D-DIA deformation experiments over a range of pressure and temperature conditions should be performed. EVPSC

modeling of these data would provide constraints on the variation in polycrystals CRSS values, slip system activities, and yield strength.

VI. CONCLUSION

In this work, the EVPSC simulation using an affine linearization assumption fits the D-DIA experiment results well, both in Q-factor and in texture evolution. From the simulation results, approximate CRSS of $\{110\}\langle 1\bar{1}0\rangle$ (1.2 GPa) and $\{110\}\langle 011\rangle$ (3.2 GPa) slip systems can be attained if using an affine linearization assumption. However, the texture does not evolve as quickly as in the experiment. If using a tangent assumption, then we can only constrain the CRSS of the $\{110\}\langle 1\bar{1}0\rangle$ slip system. The ratio of the CRSS of $\{100\}\langle 011\rangle$ to $\{110\}\langle 1\bar{1}0\rangle$ is high for the tangent approximation. All parameters including CRSS, strain hardening parameters, rate-sensitive stress exponent, initial grain shape, and linearization assumption play a role and need to be combined in order to obtain a description of lattice strain and texture evolution compatible with the ones measured in the experiment. We explain a rather unconventional dip in the evolution of the Q-factor of the {200} planes by a mechanism of dislocations unpinning from C atoms and consequent reduction in the CRSS's. Experiments and simulations for multiple D-DIA datasets under varying pressure and temperature conditions should be performed to constrain the plastic behavior of periclase under high pressure and temperature conditions. These will allow us to test predictions based on numerical modeling and to infer the plastic behavior of periclase in the deep interior of planets.

SUPPLEMENTARY MATERIAL

See supplementary material for diffraction data analysis and initial grain shape and linearization effect on the EVPSC modeling.

ACKNOWLEDGMENTS

We thank J. Amodeo and S. Dancette from MATEIS, CNRS-INSA Lyon, for suggesting dislocation pinning by impurities in MgO. D-DIA experiments were performed on beamline ID06 at the European Synchrotron Radiation Facility (ESRF), Grenoble, France. Electron microscopy experiments were performed at the electron microscopy national facility in Lille (France), supported by the Conseil Regional des Hauts de France, the European Regional Development Fund (ERDF), and the Institut National des Sciences de l'Univers (INSU, CNRS). L.M. acknowledges support from CDAC and NSF (EAR-1344579 and EAR-1654687). J.I. acknowledges support through DFG-Grant No. MA4534/4-1. H.M. is supported through the project "GeoMaX" funded under the Emmy-Noether Program of the German Science Foundation (MA4534/3-1) as well as by the Bavarian Academy of Sciences. S.M. and N.H. acknowledge support from the Programme National de Planétologie of the CNRS INSU. S.M. is also supported by the Institut Universitaire de France. This work benefited from a one-month invited professorship for C. N. Tomé at University of Lille (France). We are grateful to W. Crichton and J. Guignard at the ESRF for providing assistance in using beamline ID06 and also wish to thank D. Troadec, IEMN, CNRS, Université Lille 1, for the focused ion beam sample preparation.

Amodeo, J., Carrez, P., and Cordier, P., "Modelling the effect of pressure on the critical shear stress of MgO single crystals," Philos. Mag. **92**(12), 1523–1541 (2012).

Amodeo, J., Carrez, P., Devincre, B., and Cordier, P., "Multiscale modelling of MgO plasticity," Acta Mater. **59**(6), 2291–2301 (2011).

Amodeo, J., Dancette, S., and Delannay, L., "Atomistically-informed crystal plasticity in MgO polycrystals under pressure," Int. J. Plast. **82**, 177–191 (2016).

Appel, F. and Wielke, B., "Low temperature deformation of impure MgO single crystals," Mater. Sci. Eng. **73**, 97–103 (1985).

Barber, D. J., Wenk, H. R., Gomez-Barreiro, J., Rybacki, E., and Dresen, G., "Basal slip and texture development in calcite: New results from torsion experiments," Phys. Chem. Miner. **34**(2), 73–84 (2007).

Birch, F., "Finite elastic strain of cubic crystals," Phys. Rev. **71**(11), 809 (1947).

Bridgman, P. W., "Shearing phenomena at high pressures, particularly in inorganic compounds," Proc. Am. Acad. Arts Sci. **71**(9), 387–460 (1937).

Castelnau, O., Blackman, D. K., Lebensohn, R. A., and Castañeda, P. P., "Micromechanical modeling of the viscoplastic behavior of olivine," J. Geophys. Res.: Solid Earth **113**(B9), B09202, https://doi.org/10.1029/2007JB005444 (2008).

Copley, S. M. and Pask, J. A., "Deformation of polycrystalline MgO at elevated temperatures," J. Am. Ceram. Soc. **48**(12), 636–642 (1965).

Coppari, F., Smith, R. F., Eggert, J. H., Wang, J., Rygg, J. R., Lazicki, A., Hawreliak, J. A., Collins, T. S., and Duffy, T. S., "Experimental evidence for a phase transition in magnesium oxide at exoplanet pressures," Nat. Geosci. **6**, 926–929 (2013).

Cordier, P., Amodeo, J., and Carrez, P., "Modelling the rheology of MgO under Earth's mantle pressure, temperature and strain rates," Nature **481**(7380), 177–180 (2012).

Day, R. B. and Stokes, R. J., "Mechanical behavior of polycrystalline magnesium oxide at high temperatures," J. Am. Ceram. Soc. **49**(7), 345–355 (1966).

Duffy, T. S., Hemley, R. J., and Mao, H. K., "Equation of state and shear strength at multimegabar pressures: Magnesium oxide to 227 GPa," Phys. Rev. Lett. **74**(8), 1371 (1995).

Freund, F., "Solute carbon and carbon segregation in magnesium oxide single crystals—a secondary ion mass spectrometry study," Phys. Chem. Miner. **13**(4), 262–276 (1986).

Girard, J., Chen, J., and Raterron, P., "Deformation of periclase single crystals at high pressure and temperature: Quantification of the effect of pressure on slip-system activities," J. Appl. Phys. **111**(11), 112607 (2012).

Guignard, J. and Crichton, W. A., "The large volume press facility at ID06 beamline of the European synchrotron radiation facility as a High Pressure-High Temperature deformation apparatus," Rev. Sci. Instrum. **86**(8), 085112 (2015).

Hall, E. O., "The deformation and ageing of mild steel: III discussion of results," Proc. Phys. Soc. Sect. B **64**(9), 747 (1951).

Heidelbach, F., Stretton, I., Langenhorst, F., and Mackwell, S., "Fabric evolution during high shear strain deformation of magnesiowüstite (Mg0. 8Fe0.2O," J. Geophys. Res.: Solid Earth **108**(B3), 2154, https://doi.org/10.1029/2001JB001632 (2003).

Hulse, C. O. and Pask, J. A., "Mechanical properties of magnesia single crystals compression," J. Am. Ceram. Soc. **43**(7), 373–378 (1960).

Issa, I., Amodeo, J., Réthoré, J., Joly-Pottuz, L., Esnouf, C., Morthomas, J., and Masenelli-Varlot, K., "In situ investigation of MgO nanocube deformation at room temperature," Acta Mater. **86**, 295–304 (2015).

Kinsland, G. L. and Bassett, W. A., "Strength of MgO and NaCl polycrystals to confining pressures of 250 kbar at 25 C," J. Appl. Phys. **48**(3), 978–985 (1977).

Lebensohn, R. and Tomé, C. N., "A self-consistent viscoplastic model: Prediction of rolling textures of anisotropic polycrystals," Mater. Sci. Eng.: A **175**(1-2), 71–82 (1994).

Lebensohn, R. A., Tomé, C. N., and Castaneda, P. P., "Self-consistent modelling of the mechanical behaviour of viscoplastic polycrystals incorporating intragranular field fluctuations," Philos. Mag. **87**(28), 4287–4322 (2007).

Li, L., Weidner, D. J., Chen, J., Vaughan, M. T., Davis, M., and Durham, W. B., "X-ray strain analysis at high pressure: Effect of plastic deformation in MgO," J. Appl. Phys. **95**(12), 8357–8365 (2004).

Long, M. D., Xiao, X., Jiang, Z., Evans, B., and Karato, S. I., "Lattice preferred orientation in deformed polycrystalline (Mg, Fe) O and implications for seismic anisotropy in D," Phys. Earth Planet. Inter. **156**(1), 75–88 (2006).

Lutterotti, L., Matthies, S., Wenk, H. R., Schultz, A. S., and Richardson, Jr., J. W., "Combined texture and structure analysis of deformed limestone from time-of-flight neutron diffraction spectra," J. Appl. Phys. **81**(2), 594–600 (1997).

Marquardt, H. and Miyagi, L., "Slab stagnation in the shallow lower mantle linked to an increase in mantle viscosity," Nat. Geosci. **8**(4), 311–314 (2015).

Matthies, S. and Vinel, G. W., "On the reproduction of the orientation distribution function of texturized samples from reduced pole figures using the conception of a conditional ghost correction," Phys. Status Solidi (b) **112**(2), K111–K114 (1982).

Meade, C. and Jeanloz, R., "Yield strength of MgO to 40 GPa," J. Geophys. Res.: Solid Earth **93**(B4), 3261–3269, https://doi.org/10.1029/JB093iB04p03261 (1988).

Merkel, S., Gruson, M., Wang, Y., Nishiyama, N., and Tomé, C. N., "Texture and elastic strains in hcp-iron plastically deformed up to 17.5 GPa and 600 K: Experiment and model," Modell. Simul. Mater. Sci. Eng. **20**(2), 024005 (2012).

Merkel, S. and Hilairet, N., "Multifit/Polydefix: A framework for the analysis of polycrystal deformation using X-rays," J. Appl. Crystallogr. **48**(4), 1307–1313 (2015).

Merkel, S., Tomé, C., and Wenk, H. R., "Modeling analysis of the influence of plasticity on high pressure deformation of hcp-Co," Phys. Rev. B **79**(6), 064110 (2009).

Merkel, S., Wenk, H. R., Shu, J., Shen, G., Gillet, P., Mao, H. K., and Hemley, R. J., "Deformation of polycrystalline MgO at pressures of the lower mantle," J. Geophys. Res.: Solid Earth **107**(B11), ECV3-1, https://doi.org/10.1029/2001JB000920 (2002).

Miyagi, L., Nishiyama, N., Wang, Y., Kubo, A., West, D. V., Cava, R. J., Duffy, T. S., and Wenk, H. R., "Deformation and texture development in $CaIrO_3$ post-perovskite phase up to 6 GPa and 1300 K," Earth Planet. Sci. Lett. **268**(3), 515–525 (2008).

Paterson, M. S. and Weaver, C. W., "Deformation of polycrystalline MgO under pressure," J. Am. Ceram. Soc. **53**(8), 463–471 (1970).

Petch, N. J., "The cleavage strength of polycrystals," J. Iron Steel Inst. **174**, 25–28 (1953).

Ringwood, A. E., "Phase transformations and their bearing on the constitution and dynamics of the mantle," Geochim. Cosmochim. Acta **55**(8), 2083–2110 (1991).

Sato, F. and Sumino, K., "The yield strength and dynamic behavior of dislocations in MgO crystals at high temperature," J. Mater. Sci. **15**(7), 1625–1634 (1980).

Singh, A. K., "The lattice strains in a specimen (cubic system) compressed nonhydrostatically in an opposed anvil device," J. Appl. Phys. **73**(9), 4278–4286 (1993).

Singh, A. K., Balasingh, C., Mao, H. K., Hemley, R. J., and Shu, J., "Analysis of lattice strains measured under nonhydrostatic pressure," J. Appl. Phys. **83**(12), 7567–7575 (1998).

Sinha, M. N., Lloyd, D. J., and Tangri, K., "Dislocation dynamics and thermally-activated deformation of MgO single crystals," Philos. Mag. **28**(6), 1341–1352 (1973).

Stretton, I., Heidelbach, F., Mackwell, S., and Langenhorst, F., "Dislocation creep of magnesiowüstite ($Mg_{0.8}Fe_{0.2}O$)," Earth Planet. Sci. Lett. **194**(1), 229–240 (2001).

Tomé, C., Canova, G. R., Kocks, U. F., Christodoulou, N., and Jonas, J. J., "The relation between macroscopic and microscopic strain hardening in FCC polycrystals," Acta Metall. **32**(10), 1637–1653 (1984).

Tommaseo, C. E., Devine, J., Merkel, S., Speziale, S., and Wenk, H. R., "Texture development and elastic stresses in magnesiowűstite at high pressure," Phys. Chem. Miner. **33**(2), 84–97 (2006).

Turner, P. A. and Tomé, C. N., "A study of residual stresses in Zircaloy-2 with rod texture," Acta Metall. Mater. **42**(12), 4143–4153 (1994).

Uchida, T., Funamori, N., Ohtani, T., and Yagi, T., "Differential stress of MgO and Mg_2SiO_4 under uniaxial stress field: Variation with pressure, temperature, and phase transition," in *High Pressure Science and Technology* (World Scientific Publishing, Singapore, 1996), pp. 183–185.

Uchida, T., Wang, Y., Rivers, M. L., and Sutton, S. R., "Yield strength and strain hardening of MgO up to 8 GPa measured in the deformation-DIA with monochromatic X-ray diffraction," Earth Planet. Sci. Lett. **226**(1), 117–126 (2004).

Wang, H., Wu, P. D., Tomé, C. N., and Huang, Y., "A finite strain elastic–viscoplastic self-consistent model for polycrystalline materials," J. Mech. Phys. Solids **58**(4), 594–612 (2010a).

Wang, Y., Hilairet, N., and Dera, P., "Recent advances in high pressure and temperature rheological studies," J. Earth Sci. **21**(5), 495–516 (2010b).

Weidner, D. J., Wang, Y., and Vaughan, M. T., "Yield strength at high pressure and temperature," Geophys. Res. Lett. **21**(9), 753–756, https://doi.org/10.1029/93GL03549 (1994).

Wenk, H. R., Canova, G., Molinari, A., and Mecking, H., "Texture development in halite: Comparison of Taylor model and self-consistent theory," Acta Metall. **37**(7), 2017–2029 (1989).

Wenk, H. R., Lutterotti, L., Kaercher, P., Kanitpanyacharoen, W., Miyagi, L., and Vasin, R., "Rietveld texture analysis from synchrotron diffraction images. II. Complex multiphase materials and diamond anvil cell experiments," Powder Diffr. **29**(03), 220–232 (2014).

Wenk, H. R., Matthies, S., Donovan, J., and Chateigner, D., "BEARTEX: A Windows-based program system for quantitative texture analysis," J. Appl. Crystallogr. **31**(2), 262–269 (1998).

Wenk, H. R., Rybacki, E., Dresen, G., Lonardelli, I., Barton, N., Franz, H., and Gonzalez, G., "Dauphiné twinning and texture memory in polycrystalline quartz. Part 1: Experimental deformation of novaculite," Phys. Chem. Miner. **33**(10), 667 (2006).

Yamazaki, D. and Karato, S. I., "Fabric development in (Mg, Fe) O during large strain, shear deformation: Implications for seismic anisotropy in Earth's lower mantle," Phys. Earth Planet. Inter. **131**(3), 251–267 (2002).

Zha, C. S., Mao, H. K., and Hemley, R. J., "Elasticity of MgO and a primary pressure scale to 55 GPa," Proc. Natl. Acad. Sci. **97**(25), 13494–13499 (2000).

Zhang, S., Karato, S. I., Gerald, J. F., Faul, U. H., and Zhou, Y., "Simple shear deformation of olivine aggregates," Tectonophysics **316**(1), 133–152 (2000).